analytical chemistry

Article

Cite This: Anal. Chem. 2018, 90, 14493−14499

pubs.acs.org/ac

DNA-Walker-Induced Allosteric Switch for Tandem Signal Amplification with Palladium Nanoparticles/Metal−Organic Framework Tags in Electrochemical Biosensing

Tingting Yan, Longyi Zhu, Huangxian Ju, and Jianping Lei*

State Key Laboratory of Analytical Chemistry for Life Science, School of Chemistry and Chemical Engineering, Nanjing University, Nanjing 210023, China

Supporting Information

ABSTRACT: A DNA walker as a new molecular machine can walk on defined tracks to directly generate signal indicators in biosensing and biomedical applications. In this work, a tandem signal amplification strategy was developed on the basis of the DNA-walker-induced conformation switch for bridging palladium nanoparticles/metal−organic framework tags in ultrasensitive electrochemical DNA biosensing. The signal tags were synthesized by in situ reduction of Pd nanocrystals on porphyrinic metal−organic frameworks (PCN-224), followed by conjugation with streptavidin (SA). The as-prepared Pd/PCN-224-SA tag could electrocatalyze the oxidation of $NaBH_4$ with high efficiency for signal readout. The presence of target DNA released swing arms that were each silenced by a blocker, and then the activated swing arms could hybridize with hairpin DNA. The movement of swing arms was powered by enzymatic cleavage of conjugated oligonucleotides, inducing the allosteric switch from hairpin to SA aptamer. Therefore, Pd/PCN-224-SA tags were brought onto the electrode surface via SA-aptamer biorecognition to generate the enhanced electrochemical signal. The DNA walker-based electrochemical biosensor demonstrated good performance such as 6 orders of magnitude linear range, femtomolar detection limit, and single mismatch differentiation ability. Moreover, the feasibility of the biosensor was identified in serum matrixes. The tandem signal amplification of metal−organic frameworks and DNA walkers provided a new avenue in trace electrochemical biosensing.

DNA walkers that autonomously move along an engineered DNA track[1] have been widely applied in biosensors,[2−6] material assembly and synthesis,[7] drug-delivery,[8] and biocomputing[9] because of their remarkable locomotion, controllability, and processivity.[10] In particular, powered by toehold-mediated strand displacement[11] or DNAzyme/endonuclease-mediated hydrolysis,[12,13] the DNA walkers could walk along a track to release the indicators for signal amplification. For example, a binding-induced DNA nanomachine was proposed to move along with dye-tagged DNA on gold nanoparticles for recovering fluorescence in response to protein recongition.[14] Although the DNA-walker-based signal amplifications can directly generate electrochemical or fluorescent indicators in a single binding event, the sensitivity of the DNA walker alone is not high enough in trace analysis. Different from single signal amplification, here, we used a DNA-walker-induced conformation switch to bridge palladium nanoparticles/metal−organic framework tag as electrocatalyst for ultrasensitive electrochemical detection of DNA.

Metal−organic frameworks (MOFs) attract extensive interest and exhibit a variety of applications because of their unique properties such as high surface areas, well-defined porosities, and chemical tenability.[15−21] Typically, their permanent porosity and high chemical stability enable their inherent superiority to confine guest species for improving catalytic performance and/or the expansion of reaction scope.[22−26] Especially, because their desirable surface morphology is available for hosting metal nanoparticles, the rational integration of metal nanoparticles and MOFs effectively synergizes their respective strengths and offsets their drawbacks.[27−31] For example, in the Ag nanoparticles@zeolite-type MOF (Ag NPs@MIL-101) catalyst, MIL-101 is capable of enriching CO_2 molecules around Ag NPs, and the latter plays a role as active center to further catalyze the CO_2 addition with alkynes.[32] Because the electron-injected Pt NPs inside the UiO-66-NH_2 shell greatly shorten the electron-transport distance, Pt-decorated MOF nanocomposites (Pt@UiO-66-NH_2) exhibit significantly photocatalytic hydrogen production activity.[33] Apparently, the functional synergy between metal nanoparticles and MOFs is suitable for signal transduction in electrochemical biosensors.[34]

Palladium nanoparticles (Pd NPs) have been widely used for borohydride fuel cells, hydrogen oxidation reaction, and oxygen reduction reaction because of their strong interaction with H_2 molecules.[35−37] In this work, a tandem signal

Received: September 22, 2018
Accepted: November 26, 2018
Published: November 26, 2018

DOI: 10.1021/acs.analchem.8b04338
Anal. Chem. 2018, 90, 14493−14499

amplification strategy was developed by integrating the electrocatalysis of Pd/MOFs with DNA-walker-induced conformation switch for ultrasensitive electrochemical biosensing. First, the signal tags were synthesized by reducing the Pd precursor on the MOF (PCN-224) surface to obtain Pd/PCN-224 composite, and followed by conjugation with streptavidin (SA) as a recognition element (Scheme 1A). On the other hand, the DNA walker substrate was constructed by the covalent assembly of hairpin structures incorporated a SA aptamer sequence as the track and blocked swing arm as the walker strand on the indium tin oxide (ITO) electrode (Scheme 1B). Upon the addition of target DNA, it could hybridize with the blocker through a strand-displacement reaction, releasing swing arms from the blocker. Thus, the autonomous walking of swing arms was initiated by the nicking endonuclease (Nb·BbvCI)-catalyzed cleavage of hairpin DNA (Figure S1), which switched the track DNA conformation from hairpin structure to aptamer on the ITO electrode. The activated hairpin DNA could specifically bind to Pd/PCN-224-SA probes via biorecognition affinity between SA and its aptamer. Therefore, the electrocatalysis of Pd/PCN-224-SA tag toward $NaBH_4$ oxidation was used to produce a large electrochemical signal for DNA analysis. The electrochemical biosensor with tandem signal amplification demonstrated an excellent detection performance and good feasibility in serum samples, demonstrating a proof-of concept in biological analysis.

Scheme 1. Schematic Illustration of (A) Synthesis of Pd/PCN-224-SA Tags and (B) Tandem Signal Amplification Strategy Based on DNA-Walker-Induced Allosteric Switch and Electrocatalysis of Pd/PCN-224-SA in Electrochemical Biosensing

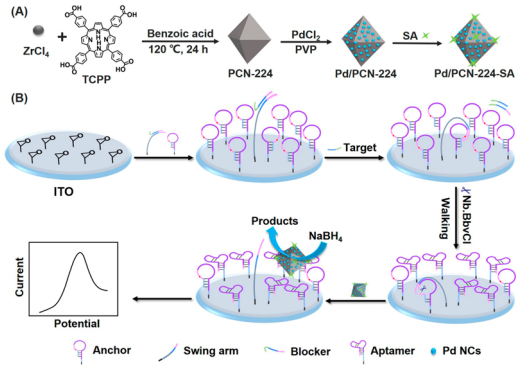

EXPERIMENTAL SECTION

Materials and Reagents. Zirconium chloride ($ZrCl_4$), palladium(II) chloride ($PdCl_2$), polyvinylpyrrolidone (PVP, MW = 55000), ethylene glycol (EG), streptavidin, (3-glycidyloxypropyl) trimethoxysilane (GOPS), and $NaBH_4$ were purchased from Sigma-Aldrich Inc. Tetrakis (4-carboxyphenyl) porphyrin (TCPP) was obtained from J&K Scientific Ltd. (China). Nb. BbvCI (10 000 U mL^{-1}) and 10× NEB buffer were purchased from New England Biolabs (Ipswich, MA). Indium tin oxide (ITO) coated glass as the electrode material was purchased from Zhuhai Kaivo Electronic Components Co., Ltd., and cut into 5.0 cm × 0.7 cm. Ten mM Tris (hydroxy-methyl)-aminomethane-HCl (Tris-HCl) containing 50 mM NaCl and 10 mM $MgCl_2$ (pH 7.4) was prepared as oligonucleotide stock solution and DNA hybridization solution. Human serum samples were obtained from Jiangsu Province Tumor Hospital. The DNA oligonucleotides in Table S1 were synthesized by Sangon Inc. (Shanghai, China).

Apparatus. Scanning electron microscope (SEM) and transmission electron microscopic (TEM) images were obtained by using an S-4800 scanning electron microscope (Hitachi, Japan) and a JEM-2100 transmission electron microscope (JEOL Ltd., Japan), respectively. X-ray diffraction (XRD) (ARL, Switzerland) and nitrogen isotherms (Micromeritics ASAP 2020) were applied to characterize the structures of PCN-224. Infrared spectra were recorded on a Vector 22 Fourier transform infrared (FT-IR) spectrometer (Bruker Optics, Germany). Cyclic voltammetry (CV) and linear sweeping voltammetry (LSV) were measured on CHI 630D electrochemical workstation (Shanghai CH Instruments, China) using a modified ITO working electrode versus a saturated calomel electrode (SCE). The contact angle system (OCA30, Dataphysic Instruments GmbH, Germany) was employed to characterize the hydrophobicity of the ITO surface. Polyacrylamide gel electrophoresis (PAGE) was carried out using into 15% native polyacrylamide hydrogel and scanned with a Molecular ImagerGel Doc XRS.

Preparation of Pd/PCN-224 and Pd/PCN-224-SA Tag. The PCN-224 was synthesized according to a previous report with some modifications.[38] The as-prepared PCN-224 (50 mg) was ultrasonically dispersed in 2.5 mL of EG and preheated at 120 °C for 10 min. Then, 94 μL of 1.12 M PVP and 47 μL of 5.64 mM $PdCl_2$ aqueous solution were added to the EG every 30 s with constant vigorous stirring (total volumes for PVP and $PdCl_2$ aqueous solutions are 3 and 1.5 mL, respectively). The resulting mixture was kept at 120 °C for an additional 10 min and then cooled to room temperature. The synthesized sample was further dried overnight at 50 °C under dynamic vacuum for further use.[39] For comparison, the Pd NPs were prepared in an aqueous solution (8.0 mL) containing 105 mg of PVP, L-ascorbic acid (60 mg), KBr (300 mg), and $PdCl_2$ (50 mg).[40] Finally, the Pd/PCN-224-SA tag was obtained via the amide reaction between NH_2 groups of SA and carboxylic acid groups of PCN-224,[34] and stored at 4 °C for further use.

Construction of Biosensor and Electrochemical Detection. The hybridization of swing arm and blocker was performed in 10 mM Tris-HCl at 37 °C for 2 h to make sure swing arm inactive. Then, 10 μL mixture of the annealed hairpin and the swing arm/blocker duplex at the certain volume ratio in 10 mM Tris-HCl was added overnight on 2% GOPS modified ITO electrode at room temperature, followed by washing with 10 mM Tris-HCl (pH = 7.4). Therefore, the hairpin and the swing arm/blocker duplex functionalized ITO as DNA walker substrate (DW-substrate) was achieved for the electrochemical detection.

Next, 6 μL of the target with varied concentrations and Nb·BbvCI were added into the above DW-substrate and then incubated at 37 °C for 2 h. Finally, the resulting electrode was immersed in 1.0 mg mL^{-1} Pd/PCN-224-SA solution at 37 °C for 1 h and then washed with 10 mM Tris-HCl. The electrochemical measurement was performed from −1.0 to 0.9 V in 0.1 M pH 11.0 H_3BO_3−NaOH in the presence of 5.0 mM $NaBH_4$ by using LSV or CV methods at a scan rate of 50 mV/s.

DOI: 10.1021/acs.analchem.8b04338
Anal. Chem. 2018, 90, 14493−14499

RESULTS AND DISCUSSION

Characterization of Pd/PCN-224 and Pd/PCN-224-SA Tag. The high-magnification SEM and TEM images clearly show the perfect cubical shapes of PCN-224 with uniform shapes (~100 nm) (Figure 1A). After Pd NPs are loaded, the crystal morphology of PCN-224 is still intact (Figure 1B), indicating that Pd NPs did not affect the cubisexualc crystal structure. Furthermore, the size distribution for the well-dispersed Pd NPs on the PCN-224 surface is mostly ~2 nm (Figure S2A and B). On the contrast, the Pd NPs (Figure S2C and D) synthesized by the typical hydrothermal method are much larger with an average size of around 10 nm.

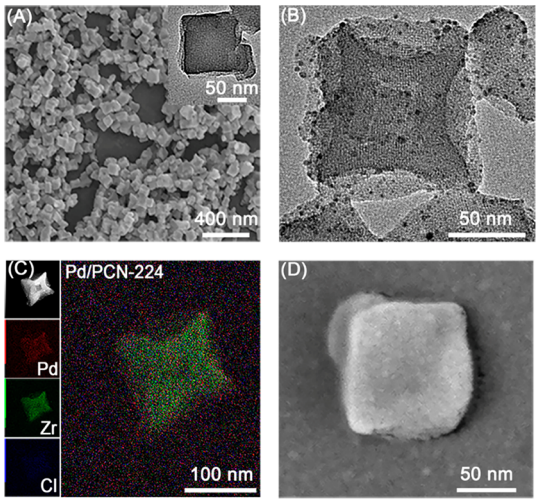

Figure 1. (A) SEM and TEM images of PCN-224. (B) TEM images and (C) EDX mapping analysis of Pd/PCN-224. (D) SEM image of Pd/PCN-224-SA.

The crystal structure of PCN-224 and Pd/PCN-224 tag was further determined using powder XRD (Figure 2A). The XRD curve shows the peaks at 4.6°, 6.5°, 7.9°, 9.2°, 11.2°, and 13.8°, which can be indexed to (200), (220), (222), (400), (422), and (600) of the cubical geometry, respectively, indicating the cubisexualc crystal structure of PCN-224 material.[38] Compared with the intrinsic PCN-224, Pd/PCN-224 shows no significant loss of crystallinity in the XRD pattern. The lattice fringes of Pd/PCN-224 display interplanar spacing of 1.89 and 1.07 nm in the particle (Figure S3A), which match well with that of (200) and (222) lattice planes of PCN-224, respectively. Moreover, the crystal structure of Pd NPs supported on the PCN-224 is in accordance with the XRD pattern of Pd NPs (Figure S3B and S4A),[40,41] which was further confirmed by the results of thermogravimetric analysis (Figure S4B).

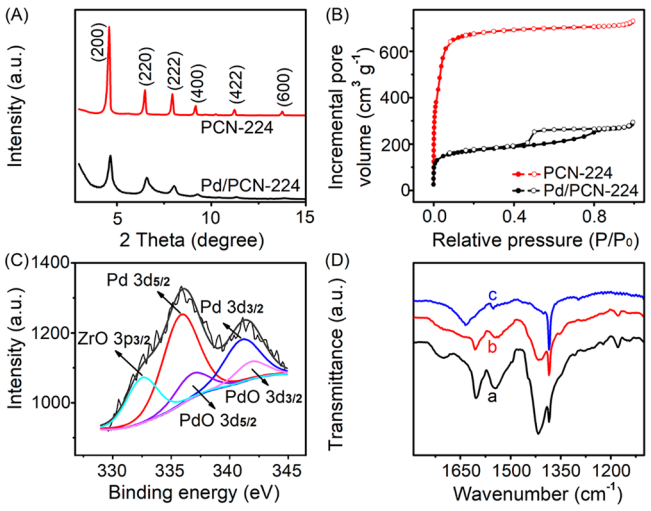

Figure 2. (A) Powder XRD patterns and (B) N_2 adsorption−desorption isotherms at 77 K of PCN-224 (red) and Pd/PCN-224 (black). (C) XPS spectra of Pd/PCN-224 composite. (D) FT-IR spectra for PCN-224 (a), Pd/PCN-224 (b), and Pd/PCN-224-SA (c).

The nitrogen adsorption−desorption curves of PCN-224 increased at low relative pressure (p/p_0 < 0.095) and reached equilibrium at medium or high relative pressure (Figure 2B), indicating an IUPAC type I structure. The N_2 adsorption−desorption curves of Pd/PCN-224 have a lower adsorption amount than that of PCN-224, while the incremental pore volume at pore width peak of 1.7 nm sharply decreased (Figure S4C), indicating the assembly of Pd NPs on the surface of PCN-224. In addition, a hysteresis loop for the typical mesoporous character was revealed with pore size range extending to 11.8 nm, which may be attributed to the remove of acetic acid during the encapsulation and washing process of Pd/PCN-224.[42]

The XPS survey spectrum further showed that Pd NPs were supported on the PCN-224 (Figure S4D), and the Pd percentage in Pd/PCN-224 was estimated to be 0.8% with the atomic ratio of Pd to Zr is 0.67. Furthermore, the fitted Pd 3d spectrum exhibits two contributions at 335.8 and 341.1 eV, which are attributed to $3d_{5/2}$ and $3d_{3/2}$ (Figure 2C), respectively.[43] In addition, the specific distribution of three elements including Pd, Zr, and Cl can be seen in Figure 1C, indicating the homogeneous decorated of Pd on the surface of PCN-224, and the corresponding result of EDS shows that the Pd/Zr atom ratio was 0.71, which is consistent with that of XPS. The total distributions of elements Pd and Zr confirmed by inductively coupled plasma were 0.087% and 1.5%, respectively. Therefore, the Pd NPs were successfully decorated on the surface of PCN-224 for the electrocatalytic activity toward $NaBH_4$ oxidation.

After functionalization of Pd/PCN-224 with SA, some agglomerates were observed on the surface of PCN-224 (Figure 1D). Furthermore, from the FT-IR spectra (Figure 2D), the peak at 1602−1603 cm^{-1} (s), ascribed to the asymmetric stretching vibration of $-COO^-$ in TCPP, was observed for both PCN-224 (curve a) and Pd/PCN-224 (curve b). However, for Pd/PCN-224-SA, a new peak could be observed at 1635 cm^{-1} (m) (curve c), which is assigned to the N−H bending vibration of acid amides. A new Soret absorption at 278 nm further confirmed the connection of SA with Pd/PCN-224 (Figure S5). Therefore, all of these above identify the successful loading of SA on the surface of Pd/PCN-224.

Feasibility of the Biosensor. The electrocatalytic activity of different electrodes toward $NaBH_4$ oxidation was measured in 0.1 M pH 11.0 H_3BO_3−NaOH buffer (Figure 3A). The Pd/PCN-224-SA with 0.087% of palladium content was chosen as the final signal tag, which can produce enough high current signal for detection (Figure S6). At the bare ITO, GOPS/ITO, and PCN-224 modified GOPS/ITO, there are no signals in response to $NaBH_4$ in the examined potential range from −1.0 to 0.9 V (curves a, b, and c). Nonetheless, at the Pd/PCN-224

DOI: 10.1021/acs.analchem.8b04338
Anal. Chem. 2018, 90, 14493−14499

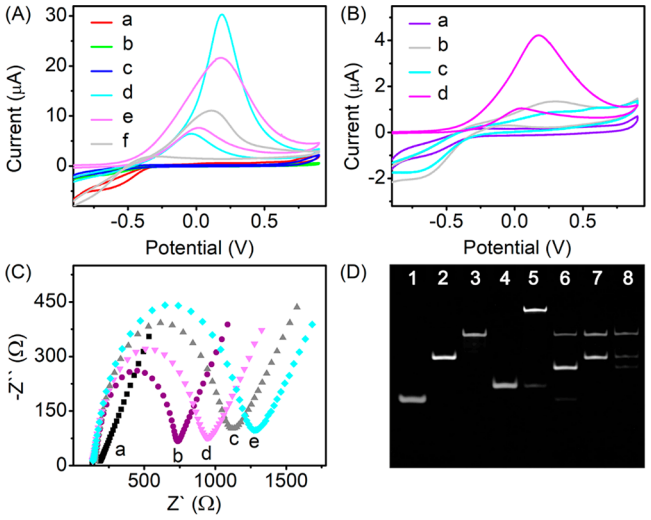

Figure 3. (A) CVs of ITO (a), GOPS/ITO (b), and PCN-224 (c), Pd/PCN-224 (d), Pd/PCN-224-SA (e), Pd NPs (f) modified GOPS/ITO in 0.1 M pH 11.0 H_3BO_3–NaOH buffer. (B) CV responses of the biosensor before (a) and after incubation with Pd/PCN-224-SA (b,d) and Pd/PCN-224 (c) in the absence (a,b) and the presence (c,d) of targets in 0.1 M pH 11.0 H_3BO_3–NaOH buffer. Scan rate: 50 mV s^{-1}. (C) EIS spectra of bare ITO (a), GOPS/ITO (b), the biosensor before (c) and after (d) incubation with target and Nb·BbvCI, (e) is (d) further incubated with Pd/PCN-224-SA in 0.1 M Na_2SO_4 solution containing a 5.0 mM $K_4[Fe(CN)_6]/K_3[Fe(CN)_6]$ (1:1) mixture. (D) PAGE analysis of 1.0 μM target (lane 1), hairpin (lane 2), swing arm (lane 3), blocker (lane 4), swing arm + blocker (lane 5), target + swing arm + blocker (lane 6), hairpin + swing arm (lane 7), and hairpin + swing arm + Nb·BbvCI (lane 8).

modified GOPS/ITO (curve d), there appeared two typical electrocatalytic peaks toward $NaBH_4$ oxidation at around 0.187 V and −0.07 V, corresponding to the oxidation of BH_4^- and the intermediate, respectively,[35] and the peak current at 0.187 V is 3.4-fold that at the Pd NPs modified ITO electrode (curve f). The enhanced electrocatalytic capacity of Pd/PCN-224 may be attributed to the synergic effect of excellent hydrogen adsorption/desorption characteristic and multielectron (maximum $8e^-$) electrocatalysis of Pd NPs toward $NaBH_4$ oxidation as well as the short electron-transport distance in porous PCN-224.[44] After conjugation with SA (curve e), the Pd/PCN-224-SA tag remained 81% of the peak current compared with that of Pd/PCN-224 modified GOPS/ITO because of the insulation of SA, which provides the sufficient current for signal readout. Moreover, the powder XRD of Pd/PCN-224 remains the original morphology after electrocatalysis for five times (Figure S7), indicating the good stability of the electrocatalyst.

The feasibility of the biosensor was investigated in the different detection conditions (Figure 3B). In the absence of target DNA and Pd/PCN-224-SA tags, the DW-substrate showed no obvious peak current in 0.1 M pH 11.0 H_3BO_3–NaOH buffer (curve a). When target DNA and Pd/PCN-224-SA tags were involved, the biosensor showed a large peak current at 0.187 V (curve d), which could be contributed to the Pd/PCN-224-SA immobilization triggered by DNA walker for electrocatalytic oxidation of $NaBH_4$. In fact, the small peak current was observed in the absence of target DNA (curve b), which was mainly attributed to the nonspecific adsorption between the Pd/PCN-224-SA and the electrode surface (Figure S8). When using Pd/PCN-224 as signal probe, there is hardly any catalytic current even in the presence of target DNA (curve c), indicating the SA is key necessary to generate the change of electrochemical signal (Figure S9).

The stepwise assembly and feasibility of the DNA walker were further studied by electrochemical impedance spectroscopic (EIS) measurements (Figure 3C), which were performed in 0.1 M KCl containing 5 mM $K_3Fe(CN)_6$ and $K_4Fe(CN)_6$. Compared with bare ITO electrode (curve a), the GOPS modified ITO showed a much larger electron-transfer resistance R_{ct} owing to the steric repulsion of GOPS (curve b). For the DW-substrate, the value of R_{ct} increased significantly because the self-assembly layer of negatively charged DNA could repel the $[Fe(CN)_6]^{3-/4-}$ to the electrode surface (curve c), which was further characterized by the contact angles (Figure S10). After the DW-substrate was treated with Nb·BbvCI and target (curve d), the R_{ct} value declined as a result of the reduction of electrostatic repulsion and steric hindrance effect, suggesting the track DNA conformation switch from hairpin to aptamer induced by DNA walker. Moreover, the R_{ct} value of the probe modified sensor increased significantly owing to the SA-aptamer biorecognition (curve e).

To evaluate feasibility of biosensing, the gel electrophoresis analysis of different migration was recorded (Figure 3D). When mixing of the swing arm (lane 3) and blocker (lane 4), a new band with slow immigration rate appears obviously due to the formation of swing arm/blocker duplex (lane 5). Upon adding target (lane 1), a new band appeared with middle immigration rate (lane 6), while the band of swing arm was recovered. This phenomenon can be explained by the fact that the target can replace the blocker to form the target/blocker duplex through the strand-displacement reaction and simultaneously release the swing arm. Sequentially, after the hybridization of hairpin and swing arm with 11 base pairs (lane 7), a new band was obtained in the presence of Nb·BbvCI (lane 8), which was attributed to the release of the aptamer sequence via the cleavage of the Nb·BbvCI endonuclease toward a double-stranded DNA substrate. The above results demonstrated the feasibility of DNA conformation switch induced by Nb·BbvCI endonuclease in the designed biosensor.

Optimization of Detection Conditions. To improve the sensitivity of the biosensor, several parameters were investigated. When the DW-substrate was incubated with target and Nb·BbvCI, the current increased at the beginning and reached a constant value after 120 min (Figure 4A). Therefore, 120 min was selected for the optimal incubation time. Then, considering the competitive effect between hairpin and swing arm/blocker duplex on the DW-substrate, the concentration ratio was optimized in Figure 4B. Apparently, the peak current increased gradually at the beginning and then reached the platform at the ratio of 20:1. Thus, the latter was chosen as the optimal ratio. According to the Cottrell equation and Faraday's law,[45−48] the density of the hairpin immobilized on the DW-substrate was estimated to be 8.7×10^{12} molecules cm^{-2} via chronocoulometry measurement using RuHex as a redox marker (Figures S11−S12). By using the ferrocene-labeled hairpin DNA to modify the electrode, the walking steps of the DNA walker were determined to be around 6 (Figure S9). Next, the length of space sequence determined by the number of thymine (T) DNA nucleotide in swing arm was investigated as shown in Figure 4C. Obviously, 40-nt T was chosen as the space sequence in swing arm for the optimal signal readout. Finally, 60 min was selected as the optimized incubation time

DOI: 10.1021/acs.analchem.8b04338
Anal. Chem. 2018, 90, 14493−14499

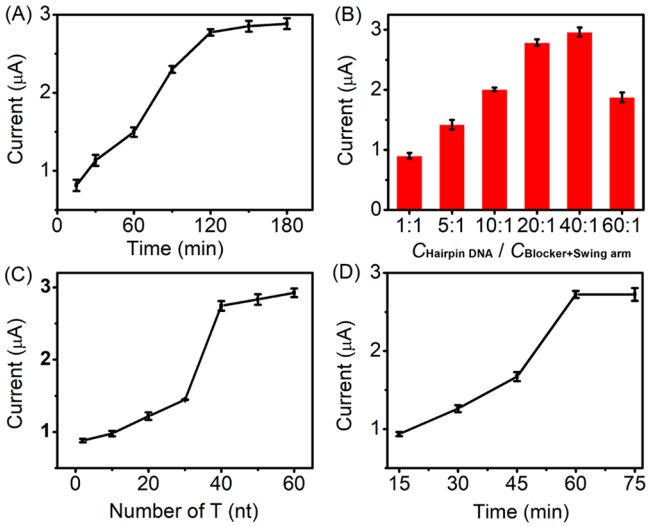

Figure 4. Dependence of electrochemical response of the biosensor on (A) incubation time in the mixture of target and Nb·BbvCI, (B) the concentration ratio of hairpin to the swing arm/blocker duplex for construction of biosensor, (C) number of T bases as spacer sequence in the swing arm, and (D) incubation time between SA aptamer and Pd/PCN-224-SA.

between SA aptamer and Pd/PCN-224-SA (Figure 4D). At the optimized conditions, the currents are 94.0% ~ 99.7% of the maximal results, providing the enough signal for the next detection.

Assay Performance. Under the optimized conditions, the enhanced catalytic currents of Pd/PCN-224-SA toward $NaBH_4$ oxidation were observed with the increasing of target DNA concentrations (Figure 5A). Additionally, the peak currents

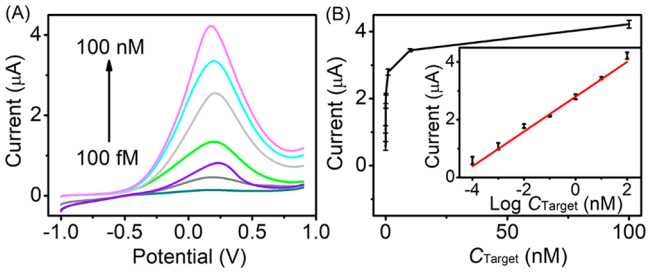

Figure 5. (A) LSV responses of the biosensor to different concentration of target DNA at 100 fM, 1 pM, 10 pM, 100 pM, 1.0 nM, 10 nM, and 100 nM (from bottom to up). (B) Dependence of peak currents on target DNA concentrations. Inset: calibration curve of current intensity vs the logarithmic value of DNA concentration.

exhibited a good proportion to the logarithm of target DNA concentration in the range from 100 fM to 100 nM with a linear equation: Current (μA) = 0.60 Log C_{Target} (nM) + 2.8 (R^2 = 0.992) (Figure 5B). The detection limit of 33.6 fM was calculated at the S/N = 3, which was lower than that of gold nanorod-based electrochemical DNA biosensor (2 pM)[49] and that of silver-dendrimer nanocomposites as oligonucleotide labels for electrochemical stripping detection of DNA (0.78 pM).[50] Moreover, this method has higher sensitivity and wider dynamic range than that of other electrochemical DNA biosensors (Table S2).

To estimate the stability of the biosensor, five independently prepared electrodes were used with the relative standard deviation (RSD) of 2.1%, showing acceptable stability and reliability. Meanwhile, the interassay precision of eight electrodes was examined with the RSD of 4.9%, indicating the acceptable fabrication reproducibility. Furthermore, the current of ITO electrode decreased to 96.4 ± 3.2% after storage at 4 °C for 15 days, showing good storage stability. After repetitive use at different aptamer-modified ITO, the Pd/PCN-224-SA tags remained 93.1% of the initial value for five times, indicating the accepted recyclable performance.

To evaluate the selectivity of the designed biosensor, the influence of different DNA sequences on current were investigated (Figure 6). The signal of single/two/three-base

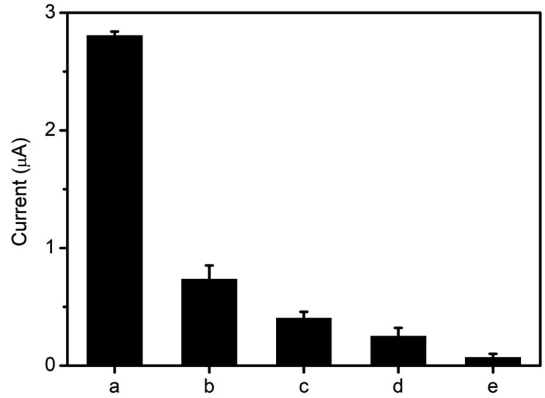

Figure 6. LSV responses of the biosensor to 1.0 nM target DNA (a), single-base (b), two-base (c), three-base (d) mismatched DNA, and random DNA (e).

mismatched sequence was 25%, 14%, and 9% of complementary target DNA, respectively. In addition, the signal of random DNA can be neglected. Overall, the high sensitivity, wide detection range, and good selectivity of the designed biosensor indicated its great potential application.

Real Sample Analysis. The analytical reliability and potential application of the proposed biosensor were further analyzed with the recovery test in clinical samples. By adding 1 pM and 10 nM standard target solution into 10% (v/v) human serum samples, the recoveries were 98.0 ± 4.6% and 106.0 ± 3.9%, respectively, indicating the acceptable feasibility of the proposed method for the detection of complex biological samples.

CONCLUSIONS

In summary, we successfully designed a tandem signal amplification strategy based on the DNA-walker-induced conformation switch to immobilize Pd/PCN-224 electrocatalyst for ultrasensitive electrochemical detection of DNA. The conjugation of Pd NPs with PCN-224 not only avoided the aggregation of Pd NPs but also took advantage of the hydrogen adsorption/desorption characteristic of Pd NPs and the short electron-transport distance of porous PCN-224, displaying excellent catalytic activity toward $NaBH_4$ oxidation. Meanwhile, upon addition of target, the DNA walker was powered by Nb·BbvCI, and the movement of swing arms induced the allosteric switch of hairpin DNA to produce thermodynamically stable SA aptamer,[51,52] leading to the attachment of Pd/PCN-224-SA tag on the electrode surface via the specific protein-aptamer recognition. Thus, the tandem

DOI: 10.1021/acs.analchem.8b04338
Anal. Chem. 2018, 90, 14493−14499

signal amplification system demonstrated good performance such as a wide detection range, low detection limit, and good discrimination toward single-base mismatched oligonucleotide. Therefore, this work provides a new example on tandem signal amplification of multifunctional metal−organic frameworks and DNA walkers for highly sensitive and selective electrochemical biosensing.

■ ASSOCIATED CONTENT

Supporting Information

The Supporting Information is available free of charge on the ACS Publications website at DOI: 10.1021/acs.analchem.8b04338.

Corresponding illustration of the process of DNA-walker-induced allosteric switch, size distribution of Pd NPs, characterizations of Pd/PCN-224 and Pd/PCN-224-SA, effect of palladium content on electrocatalysis, stability of electrochemical tags, nonspecific adsorption, analysis on the role of SA, contact angles of ITO, calculation of the density of hairpin DNA on electrode (PDF)

■ AUTHOR INFORMATION

Corresponding Author

*E-mail: jpl@nju.edu.cn. Tel.: +86-25-89681922.

ORCID

Longyi Zhu: 0000-0002-0898-4804

Huangxian Ju: 0000-0002-6741-5302

Jianping Lei: 0000-0002-3594-180X

Notes

The authors declare no competing financial interest.

■ ACKNOWLEDGMENTS

This research was supported by the National Key Technologies R&D Program (2016YFC0302500), National Natural Science Foundation of China (21675084, 21635005, 21605082), and Natural Science Foundation of Jiangsu Province (BK20160641).

■ REFERENCES

(1) Bath, J.; Turberfield, A. J. *Nat. Nanotechnol.* **2007**, *2*, 275−284.
(2) Yang, X. L.; Tang, Y. N.; Mason, S. D.; Chen, J. B.; Li, F. *ACS Nano* **2016**, *10*, 2324−2330.
(3) Xu, Z. Q.; Liao, L. L.; Chai, Y. Q.; Wang, H. J.; Yuan, R. *Anal. Chem.* **2017**, *89*, 8282−8287.
(4) He, M. Q.; Wang, K.; Wang, W. J.; Yu, Y. L.; Wang, J. H. *Anal. Chem.* **2017**, *89*, 9292−9298.
(5) Qu, X. M.; Zhu, D.; Yao, G. B.; Su, S.; Chao, J.; Liu, H. J.; Zuo, X. L.; Wang, L. H.; Shi, J. Y.; Wang, L. H.; Huang, W.; Pei, H.; Fan, C. H. *Angew. Chem., Int. Ed.* **2017**, *56*, 1855−1858.
(6) Peng, H. Y.; Li, X. F.; Zhang, H. Q.; Le, X. C. *Nat. Commun.* **2017**, *8*, 14378.
(7) He, Y.; Liu, D. R. *Nat. Nanotechnol.* **2010**, *5*, 778−782.
(8) Li, F. R.; Cha, T. G.; Pan, J.; Ozcelikkale, A.; Han, B.; Choi, J. H. *ChemBioChem* **2016**, *17*, 1138−1141.
(9) Gilbert, D.; Heiner, M.; Rohr, C. *Nat. Comput.* **2018**, *17*, 161−182.
(10) von Delius, M.; Leigh, D. A. *Chem. Soc. Rev.* **2011**, *40*, 3656−3676.
(11) Omabegho, T.; Sha, R.; Seeman, N. C. *Science* **2009**, *324*, 67−71.
(12) Yehl, K.; Mugler, A.; Vivek, S.; Liu, Y.; Zhang, Y.; Fan, M. Z.; Weeks, E. R.; Salaita, K. *Nat. Nanotechnol.* **2016**, *11*, 184−190.
(13) Chen, Y.; Xiang, Y.; Yuan, R.; Chai, Y. Q. *Nanoscale* **2015**, *7*, 981−986.
(14) Zhang, H. Q.; Lai, M. D.; Zuehlke, A.; Peng, H. Y.; Li, X. F.; Le, X. C. *Angew. Chem., Int. Ed.* **2015**, *54*, 14326−14330.
(15) Li, H.; Eddaoudi, M.; O'Keeffe, M.; Yaghi, O. M. *Nature* **1999**, *402*, 276−279.
(16) Carrington, E. J.; McAnally, C. A.; Fletcher, A. J.; Thompson, S. P.; Warren, M.; Brammer, L. *Nat. Chem.* **2017**, *9*, 882−889.
(17) Wu, M. X.; Yang, Y. W. *Adv. Mater.* **2017**, *29*, 1606134.
(18) Kim, H.; Yang, S.; Rao, S. R.; Narayanan, S.; Kapustin, E. A.; Furukawa, H.; Umans, A. S.; Yaghi, O. M.; Wang, E. N. *Science* **2017**, *356*, 430−434.
(19) Lustig, W. P.; Mukherjee, S.; Rudd, N. D.; Desai, A. V.; Li, J.; Ghosh, S. K. *Chem. Soc. Rev.* **2017**, *46*, 3242−3285.
(20) Cheng, H. J.; Zhang, L.; He, J.; Guo, W. J.; Zhou, Z. Y.; Zhang, X. J.; Nie, S. M.; Wei, H. *Anal. Chem.* **2016**, *88*, 5489−5497.
(21) Fu, S. F.; Zhu, C. Z.; Song, J. H.; Du, D.; Lin, Y. H. *Adv. Energy Mater.* **2017**, *7*, 1700363.
(22) Mahmood, A.; Guo, W. H.; Tabassum, H.; Zou, R. Q. *Adv. Energy Mater.* **2016**, *6*, 1600423.
(23) Qin, J. S.; Yuan, S.; Lollar, C.; Pang, J. D.; Alsalme, A.; Zhou, H. C. *Chem. Commun.* **2018**, *54*, 4231−4249.
(24) Yin, H. Q.; Yang, J. C.; Yin, X. B. *Anal. Chem.* **2017**, *89*, 13434−13440.
(25) Liu, X.; Qi, W.; Wang, Y. F.; Su, R. X.; He, Z. M. *Nanoscale* **2017**, *9*, 17561−17570.
(26) Wang, K. C.; Feng, D. W.; Liu, T. F.; Su, J.; Yuan, S.; Chen, Y. P.; Bosch, M.; Zou, X. D.; Zhou, H. C. *J. Am. Chem. Soc.* **2014**, *136*, 13983−13986.
(27) Yang, Q. H.; Xu, Q.; Jiang, H. L. *Chem. Soc. Rev.* **2017**, *46*, 4774−4808.
(28) Chen, L. Y.; Luque, R.; Li, Y. W. *Chem. Soc. Rev.* **2017**, *46*, 4614−4630.
(29) Yang, Q. H.; Xu, Q.; Yu, S. H.; Jiang, H. L. *Angew. Chem., Int. Ed.* **2016**, *55*, 3685−3689.
(30) Zhao, M. T.; Yuan, K.; Wang, Y.; Li, G. D.; Guo, J.; Gu, L.; Hu, W. P.; Zhao, H. J.; Tang, Z. Y. *Nature* **2016**, *539*, 76−80.
(31) Huang, G.; Yang, Q. H.; Xu, Q.; Yu, S. H.; Jiang, H. L. *Angew. Chem., Int. Ed.* **2016**, *55*, 7379−7383.
(32) Liu, X. H.; Ma, J. G.; Niu, Z.; Yang, G. M.; Cheng, P. *Angew. Chem., Int. Ed.* **2015**, *54*, 988−991.
(33) Xiao, J. D.; Shang, Q. C.; Xiong, Y. J.; Zhang, Q.; Luo, Y.; Yu, S. H.; Jiang, H. L. *Angew. Chem., Int. Ed.* **2016**, *55*, 9389−9393.
(34) Ling, P. H.; Lei, J. P.; Zhang, L.; Ju, H. X. *Anal. Chem.* **2015**, *87*, 3957−3963.
(35) Simões, M.; Baranton, S.; Coutanceau, C. *J. Phys. Chem. C* **2009**, *113*, 13369−13376.
(36) Das, J.; Kim, H.; Jo, K.; Park, K. H.; Jon, S.; Lee, K.; Yang, H. *Chem. Commun.* **2009**, *49*, 6394−6396.
(37) de Leon, C. P.; Walsh, F. C.; Pletcher, D.; Browning, D. J.; Lakeman, J. B. *J. Power Sources* **2006**, *155*, 172−181.
(38) Feng, D. W.; Chung, W. C.; Wei, Z. W.; Gu, Z. Y.; Jiang, H. L.; Chen, Y. P.; Darensbourg, D. J.; Zhou, H. C. *J. Am. Chem. Soc.* **2013**, *135*, 17105−17110.
(39) Chen, Y. Z.; Wang, Z. Y. U.; Wang, H. W.; Lu, J. L.; Yu, S. H.; Jiang, H. L. *J. Am. Chem. Soc.* **2017**, *139*, 2035−2044.
(40) Li, G. Q.; Kobayashi, H.; Taylor, J. M.; Ikeda, R.; Kubota, Y.; Kato, K.; Takata, M.; Yamamoto, T.; Toh, S.; Matsumura, S.; Kitagawa, H. *Nat. Mater.* **2014**, *13*, 802−806.
(41) Zhao, M. T.; Deng, K.; He, L. C.; Liu, Y.; Li, G. D.; Zhao, H. J.; Tang, Z. Y. *J. Am. Chem. Soc.* **2014**, *136*, 1738−1741.
(42) Cai, G. R.; Jiang, H. L. *Angew. Chem., Int. Ed.* **2017**, *56*, 563−567.
(43) Tressaud, A.; Khairoun, S.; Touhara, H.; Watanabe, N. *Z. Anorg. Allg. Chem.* **1986**, *540*, 291−299.
(44) Bai, Y.; Dou, Y. B.; Xie, L. H.; Rutledge, W.; Li, J. R.; Zhou, H. C. *Chem. Soc. Rev.* **2016**, *45*, 2327−2367.
(45) Anson, F. C.; Osteryoung, R. A. *J. Chem. Educ.* **1983**, *60*, 293−296.

DOI: 10.1021/acs.analchem.8b04338
Anal. Chem. 2018, 90, 14493−14499

(46) Steel, A. B.; Herne, T. M.; Tarlov, M. J. *Anal. Chem.* **1998**, *70*, 4670−4677.
(47) Yao, B.; Liu, Y. C.; Tabata, M.; Zhu, H. T. Z.; Miyahara, Y. J. *Chem. Commun.* **2014**, *50*, 9704−9706.
(48) Zhu, J.; Gan, H. Y.; Wu, J.; Ju, H. X. *Anal. Chem.* **2018**, *90*, 5503−5508.
(49) Shakoori, Z.; Salimian, S.; Kharrazi, S.; Adabi, M.; Saber, R. *Anal. Bioanal. Chem.* **2015**, *407*, 455−461.
(50) Jin, X.; Zhou, L.; Zhu, B.; Jiang, X.; Zhu, N. N. *Biosens. Bioelectron.* **2018**, *107*, 237−243.
(51) Bing, T.; Yang, X. J.; Mei, H. C.; Cao, Z. H.; Shangguan, D. H. *Bioorg. Med. Chem.* **2010**, *18*, 1798−1805.
(52) Song, Y. L.; Cui, L.; Wu, J.; Zhang, W. T.; Zhang, W. Y.; Kang, H. Z.; Yang, C. Y. J. *Chem. - Eur. J.* **2011**, *17*, 9042−9046.

DOI: 10.1021/acs.analchem.8b04338
Anal. Chem. 2018, 90, 14493−14499